Analysis and design of a concurrent dual–band self–oscillating mixer

M. Pontón[1], A. Herrera[2], A. Suárez[3]
University of Cantabria, Spain
[1]mabel.ponton@unican.es, [2]herreraa@unican.es, [3]suareza@unican.es

***Abstract*—A concurrent dual–band self–oscillating mixer, based on a ring resonator, is proposed and analyzed in detail. Taking advantage of the ring even and odd resonances, it is able to operate in concurrent dual quasi–periodic mode and in an injection–locked regime. In the second case, it behaves as a dual frequency zero–IF mixer. The stability properties are analyzed with a reduced–order determinant function that overcomes the problem of limited observability due to a high isolation between different circuit sections. Various procedures, enabling the calculation of the conversion gain, injection–locking bandwidths and phase–noise spectral density, have been applied to a dual mixer at the frequencies 2.3 GHz and 4.1 GHz.**

***Keywords*—dual oscillator, phase noise, self–oscillating mixer, stability.**

I. Introduction

Concurrent dual–frequency oscillators enable a reduction of circuit size and weight, and are interesting for the implementation of multi–standard and multi–band wireless systems. Various configurations have been presented [1]–[4], and a major challenge is to obtain a reliable concurrent operation in sufficiently broad intervals of the circuit parameters. The concurrent oscillations correspond to a doubly autonomous quasi–periodic solution at the two incommensurate fundamental frequencies ω_1 and ω_2, which mathematically coexists with two periodic solutions, one at each of the two fundamental frequencies, and with the DC solution. For a reliable concurrent operation, the quasi–periodic solution at ω_1 and ω_2 must be the only stable one. As shown in [3]–[4], isolating the stable quasi–periodic solution from the stable periodic ones is not an easy task. In [4] this is achieved at the expense of its coexistence with the stable DC solution, which prevents the oscillations start–up from the noise level.

Recently, a concurrent dual oscillator based on a ring resonator has been proposed [5]. It takes advantage of the ring even and odd resonances to obtain the concurrent oscillations at ω_1 and ω_2 with excellent isolation. On the other hand, the ring exhibits a high quality factor, which should enable a low phase–noise spectral density. Fig. 1(a) shows the geometrical parameters of the ring resonator, based on [5]. Mode 1 (2) corresponds to transmission from Port 1 (Port 2) to Port 3 (Port 4). The resonance frequencies are established by choosing the impedances Z_1 and Z_2 in Fig. 1(a), which is done by setting the impedance ratio according to the desired oscillation frequencies $f_1 = \omega_1/(2\pi)$ and $f_2 = \omega_2/(2\pi)$, using the expression [5]:

$$\Delta f_o / f_o = 4/\pi \tan^{-1}\sqrt{Z_2/Z_1} - \tan^{-1}\sqrt{Z_1/Z_2} \qquad (1)$$

where $f_o = (f_1 + f_2)/2$ and $\Delta f_o = |f_2 - f_1|$. On the other hand, the gaps S_1 and S_2 affect the coupling strength [5].

One of the objectives of this work is to perform an in–depth stability analysis of the steady–state solutions that mathematically coexist in the ring–resonator circuit. We propose the use of a new reduced–order determinant that globally accounts for the two distinct circuit sections and overcomes the problem of limited observability in pole–zero identification [6]. A concurrent dual–band self–oscillating mixer (SOM) is implemented and analysed for the first time to our knowledge. Its two carrier frequencies are 2.3 GHz and 4.1 GHz and it can operate in two different modes: as a dual–IF SOM and under concurrent dual injection locking. The first mode constitutes an extension of the recently proposed Zero–IF SOM [7] to concurrent dual operation.

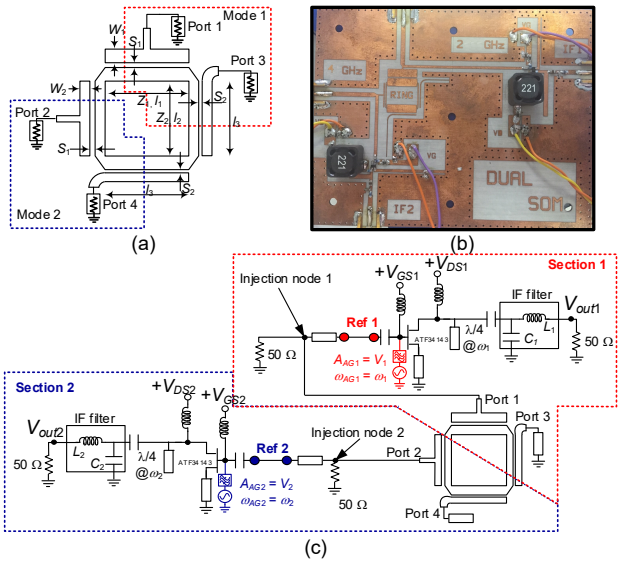

Fig. 1. Concurrent dual oscillator. (a) Geometrical parameters of the ring resonator, based on [5]. (b) Prototype built on Rogers 4003C substrate. (c) Proposed dual–frequency self–oscillating mixer for operation in concurrent dual quasi–periodic mode and concurrent dual injection–locked regime.

II. Concurrent Dual–Frequency Oscillator

The circuit in Fig. 1(b)–(c) is intended to operate as a dual SOM. The ring resonator, enabling a high quality factor, is the largest circuit component and is shared, as in [5], by two active subnetworks, implemented to fulfill the oscillation conditions at ω_1 and ω_2, respectively. The output of each subnetwork includes an open–circuited $\lambda/4$ transmission line at the corresponding oscillation frequency, as well as a low–pass filter.

In the presence of the ring resonator, and due to insufficient observability, the widely used (and accurate) pole–zero identification method [6] fails to globally account for the stability properties of the complete structure. When the transfer

function (to be identified) is calculated in a given section [Fig. 1(c)], it fails to detect the instability of the other section(s). To cope with this problem, a Nyquist analysis [8] is proposed here. In small signal, a reduced–order characteristic determinant is obtained by defining a 2x2 total impedance (admittance) matrix at two suitable analysis ports. The criterion to select these ports is the following. When terminated in an open circuit (a short circuit) [for an impedance (admittance) analysis] the active subnetworks must be stable. In the case of the circuit in Fig. 1(c), this is fulfilled at the ports indicated as Ref 1 and Ref 2. When open circuited, the active subnetworks are stable for all the gate–bias voltages, as shown in Fig. 2(a) and (b). The input impedance of the two active subnetworks, seen from Ref 1 and Ref 2, is Z_1 and Z_2, respectively. Then, the determinant of the total impedance matrix (*characteristic* determinant [9]) is:

$$\det(s) = \det\left\{\begin{bmatrix} Z_1(s) & 0 \\ 0 & Z_2(s) \end{bmatrix} + \begin{bmatrix} z_{11}(s) & z_{12}(s) \\ z_{21}(s) & z_{22}(s) \end{bmatrix}\right\} = 0 \qquad (2)$$

where s is the complex frequency and $[z_{ij}]$ is the impedance matrix of the whole passive part (including the ring resonator), with its two ports defined between the nodes in Ref 1 and Ref 2 and ground. The system poles are the roots of (2), which due to the complexity of the structure, cannot be solved in terms of s. Instead, the Nyquist criterion will be applied, analyzing $\det(j\omega)$. The number N of clockwise encirclements of $\det(j\omega)$ around the origin agrees with the difference between the number Z of right–hand side (RHS) zeroes of $\det(s)$ (agreeing with the circuit unstable poles) and the number P of RHS poles of $\det(s)$, that is, $N = Z - P$. Thus, for the Nyquist criterion to be applicable, one must have $P = 0$. The RHS poles could only come from the active impedances Z_1 and Z_2. However, because the two active circuits defined at Ref 1 and Ref 2 are stable under open–circuit terminations, Z_1 and Z_2 cannot have any RHS poles. On the other hand, a passive impedance matrix (like z_{ij}) cannot exhibit any unstable poles. Thus, the Nyquist criterion is applicable. The Nyquist plot in Fig. 2(c), for $V_{GS1} = -0.6$ V, $V_{GS2} = -3$ V, exhibits one clockwise turn about the origin due to an instability at 2.3 GHz. The plot in Fig. 2(d), for $V_{GS1} = -0.6$ V, $V_{GS2} = -0.7$ V, exhibits two turns, due to the instabilities at 2.3 GHz and 4.1 GHz.

The determinant in (2) constitutes a complete representation of the system dynamics that, by construction, cannot exhibit any RHS poles. It has two advantages: it copes with the problem of lack of observability and, if identified, it will not suffer from any uncertainties due to numerical pole–zero cancellations. Here this identification of a determinant function is carried out for the first time to our knowledge. Fig. 2(e) and Fig. 2(f) present the identification of the function $\det(j\omega)$ considered in the Nyquist plots of (c) and (d). The system poles (zeroes of the determinant), are neatly identified in the two cases. Fig. 2(g) presents the variation of the real part of the zeroes of $\det(s)$ when varying V_{GS1} for $V_{GS2} = -0.7$ V. The pair of poles at about 4.1 GHz is always on the RHS and the pair at about 2.3 GHz is on the RHS in a certain V_{GS1} interval.

When considering variations in two relevant parameters, such as V_{GS1} and V_{GS2}, the Hopf bifurcation loci will provide the pairs of parameter values at which each of the two oscillations is generated from DC. Because the oscillations are generated from zero amplitude, the loci are directly obtained by doing $s = j\omega$ in (2) and solving $\det(j\omega, V_{GS1}, V_{GS2}) = 0$ for V_{GS1} and V_{GS2}. For an exhaustive calculation, the contour–intersection method in [10] has been applied to $\det(j\omega, V_{GS1}, V_{GS2}) = 0$. Fig. 3(a) [Fig. 3(b)] shows the intersections of the contours $\mathrm{Re}[\det(j\omega)] = 0$ and $\mathrm{Im}[\det(j\omega)] = 0$ in the planes (ω, V_{GS1}) and (ω, V_{GS2}). In each case, only two intersection points are obtained. Due to the good isolation, the oscillation onset and extinction depends only on the bias voltage in each circuit section. When increasing the gate–bias voltages, the oscillation at about 2.3 GHz (about 4.1 GHz) is generated at $V_{GS1} = -0.08$ V ($V_{GS2} = -0.3$ V) and extinguished at $V_{GS1} = -0.63$ V ($V_{GS2} = -0.88$ V). This has been verified experimentally as shown later.

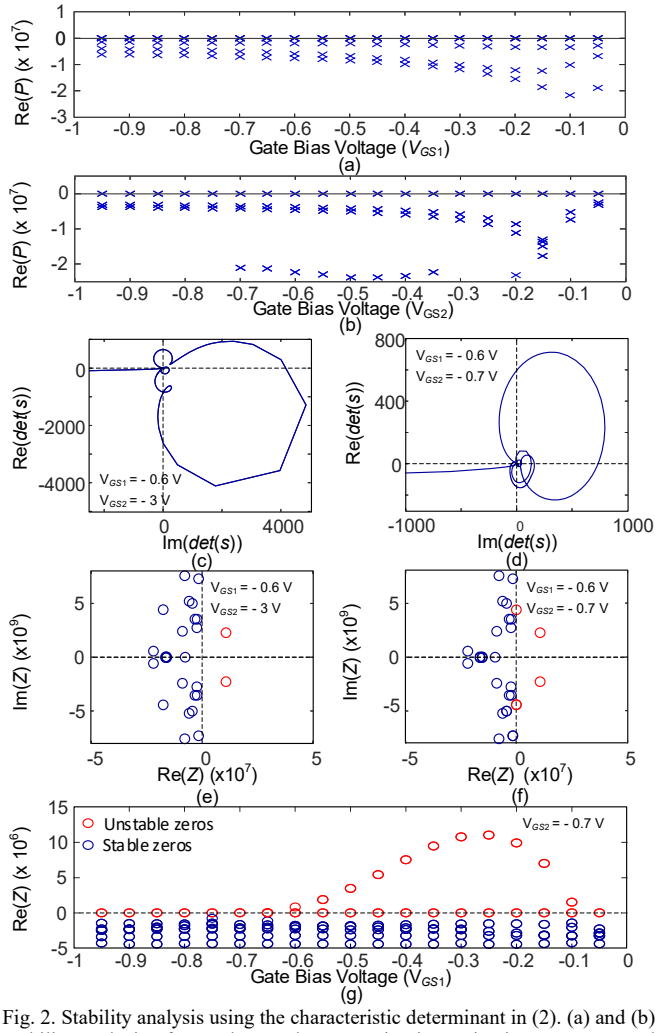

Fig. 2. Stability analysis using the characteristic determinant in (2). (a) and (b) Stability analysis of Z_1 and Z_2 under open–circuit terminations, vs. V_{GS1} and V_{GS2}, respectively. (c) Nyquist plot at $V_{GS1} = -0.6$ V and $V_{GS2} = -3$ V. (d) Nyquist plot at $V_{GS1} = -0.6$ V and $V_{GS2} = -0.7$ V. (e) and (f) Pole–zero identification of $\det(j\omega)$ in the same two cases. The zeroes provide the stability properties. (g) Evolution of the real part of the zeroes of $\det(s)$ vs. V_{GS1} while keeping $V_{GS2} = -0.7$ V.

The quasi–periodic solution at ω_1 and ω_2 is calculated with harmonic balance (HB) through the simultaneous connection of two auxiliary generators (AGs) [9], one in each section [Fig.

1(c)]. The two AGs operate at the respective frequencies ω_1 and ω_2, with the amplitudes V_1 and V_2, and must fulfill:

$$Y_{AG,1}(V_1, V_2, \omega_1, \omega_2) = 0$$
$$Y_{AG,2}(V_1, V_2, \omega_1, \omega_2) = 0 \quad (3)$$

where $Y_{AG,i}$ is the current to voltage ratio of the corresponding AG. The two–tone HB simulation is carried out with a diamond truncation of nonlinearity order NL = 5. In Fig. 4, the doubly autonomous quasi–periodic solution is compared with the experimental spectrum. Measured spectra have been obtained combining the signals at the two injections nodes in Fig. 1(c), through a power combiner with insertion loss above 6.0 dB. Fig. 4(a) shows the concurrent oscillations obtained for $V_{GS1} = -0.6$ V and $V_{GS2} = -0.7$ V. In Fig. 4 (b), for $V_{GS1} = 0.0$ V and $V_{GS2} = -0.7$ V, the oscillation at 2.3 GHz extinguishes in full agreement with the stability analysis of Fig. 2.

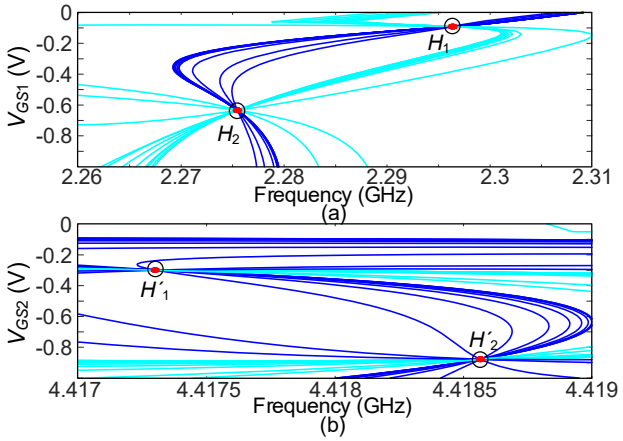

Fig. 3. Hopf bifurcations detected through the intersections of the contours: Re[det($j\omega$)] = 0 and Re[det($j\omega$)] = 0. (a) In the plane ω and V_{GS1}. (b) ω and V_{GS2}.

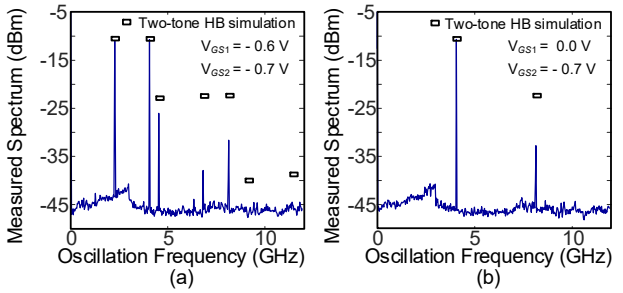

Fig. 4. Comparison between the simulated and measured doubly–autonomous quasi–periodic solution at (a) $V_{GS1} = -0.6$ V and $V_{GS2} = -0.7$ V, (b) $V_{GS1} = 0.0$ V and $V_{GS2} = -0.7$ V.

TABLE I
Coefficients determining the stability of the quasi–periodic solution

λ_1	λ_2	a_{11}	a_{12}	a_{21}	a_{22}
$-2.75\cdot10^7$	$-7.92\cdot10^8$	$-3.96\cdot10^8$	-554477	7175.3	$-1.37\cdot10^7$

The stability of the quasi–periodic solution is analyzed linearizing the two outer–tier admittance functions in (3) about the quasi–periodic steady–state solution, as done in [4]. These provide four Lyapunov exponents. Two of them are zero due to the double autonomy of this solution. The other two exponents, $\lambda_{1,2}$, determining the stability properties, are:

$$\lambda_{1,2} = \frac{a_{11} + a_{22}}{2} \pm \frac{\sqrt{(a_{11} - a_{22})^2 + 4a_{12}a_{21}}}{2} \quad (4)$$

where:

$$a_{11} = \frac{-\left(\frac{\partial Y_{T1}^r}{\partial V_1}\frac{\partial Y_{T1}^i}{\partial \omega_1} - \frac{\partial Y_{T1}^r}{\partial \omega_1}\frac{\partial Y_{T1}^i}{\partial V_1}\right)}{\left|\partial Y_{T1}/\partial \omega_1\right|^2},\quad a_{12} = \frac{-\left(\frac{\partial Y_{T1}^r}{\partial V_2}\frac{\partial Y_{T1}^i}{\partial \omega_1} - \frac{\partial Y_{T1}^r}{\partial \omega_1}\frac{\partial Y_{T1}^i}{\partial V_2}\right)}{\left|\partial Y_{T1}/\partial \omega_1\right|^2}$$

$$a_{21} = \frac{-\left(\frac{\partial Y_{T2}^r}{\partial V_1}\frac{\partial Y_{T2}^i}{\partial \omega_2} - \frac{\partial Y_{T2}^r}{\partial \omega_2}\frac{\partial Y_{T2}^i}{\partial V_1}\right)}{\left|\partial Y_{T2}/\partial \omega_2\right|^2},\quad a_{22} = \frac{-\left(\frac{\partial Y_{T2}^r}{\partial V_2}\frac{\partial Y_{T2}^i}{\partial \omega_2} - \frac{\partial Y_{T2}^r}{\partial \omega_2}\frac{\partial Y_{T2}^i}{\partial V_2}\right)}{\left|\partial Y_{T2}/\partial \omega_2\right|^2}$$

The two circuit sections in Fig. 1(c) would be fully isolated for $a_{12} = 0$ and $a_{21} = 0$ and the two exponents would become $\lambda_1 = a_{11}$ and $\lambda_2 = a_{22}$. The coefficients a_{12} and a_{21} give a measure of the connectivity between the two circuit sections. Table I presents the values of the various coefficients corresponding to the quasi–periodic solution in Fig. 4(a).

III. Concurrent Dual–Band Self–Oscillating Mixer

The dual–band SOM is obtained by concurrently mixing each oscillation frequency ω_1 (ω_2) with its own input RF signal ω_{RF1} (ω_{RF2}) [Fig. 1(c)], which provides two distinct IF signals. Under small–signal inputs, constant conversion–gain contours can be traced in the plane defined by two parameters. This is done in the presence of the two AGs. If the two parameters correspond to a same circuit section (1 or 2), the gain contours associated with that section can be traced without optimizing the AG in the other section (2 or 1). Results for an IF frequency of 100 MHz versus the output filter parameters L_1, C_1 and L_2, C_2 are shown in Fig. 5(a) and 5(b), respectively. The selected operation points are P_1 and P_2. The experimental concurrent conversion gain was –14 dB and –8 dB respectively.

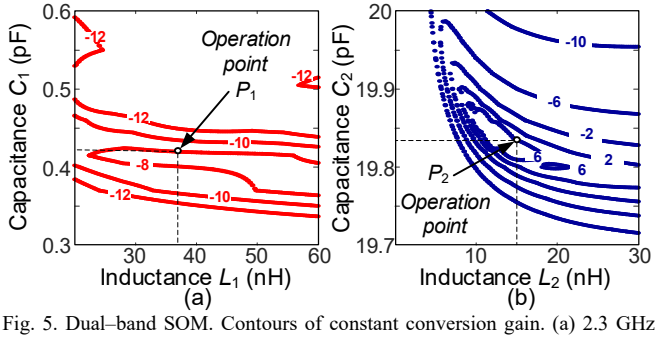

Fig. 5. Dual–band SOM. Contours of constant conversion gain. (a) 2.3 GHz band, in the plane L_1, C_1. (b) 4.1 GHz band, in the plane L_2, C_2.

A Zero–IF SOM was recently proposed [7] and is based on the injection–locking of an oscillator circuit with enhanced frequency–mixing capability, achieved by suitably biasing the active devices. This operation principle will be extended here to the concurrent dual–band oscillator. This requires an initial calculation of the concurrent injection–locking bands of the oscillators to their respective input sources, with the voltage amplitudes E_{g1} and E_{g2}. As in [7], small–signal injection levels will be used, so it will be possible to linearize the total admittance function $Y_{AG,i}$ of each oscillator about its corresponding free–running solution, obtained through (3). To account for the possible impact of one oscillator on the other,

the set of four state variables $V_1, V_2, \omega_1, \omega_2$ is considered in the linearization, which provides:

$$\begin{aligned}
&\frac{\partial Y_{AG,1}}{\partial V_1}\Delta V_1+\frac{\partial Y_{AG,1}}{\partial V_2}\Delta V_2+\frac{\partial Y_{AG,1}}{\partial \omega_1}\Delta\omega_1+\frac{\partial Y_{AG,1}}{\partial \omega_2}\Delta\omega_2+\\
&\frac{\partial Y_{AG,1}}{\partial E^r_{g1}}E_{g1}\cos\phi_1-\frac{\partial Y_{AG,1}}{\partial E^{im}_{g1}}E_{g1}\sin\phi_1=0\\
&\frac{\partial Y_{AG,2}}{\partial V_1}\Delta V_1+\frac{\partial Y_{AG,2}}{\partial V_2}\Delta V_2+\frac{\partial Y_{AG,2}}{\partial \omega_1}\Delta\omega_1+\frac{\partial Y_{AG,2}}{\partial \omega_2}\Delta\omega_2+\\
&\frac{\partial Y_{AG,2}}{\partial E^r_{g2}}E_{g2}\cos\phi_2-\frac{\partial Y_{AG,2}}{\partial E^{im}_{g2}}E_{g2}\sin\phi_2=0
\end{aligned} \tag{5}$$

where the superscripts "*r*" and "*im*" indicate real and imaginary parts, Δ indicates increments with respect to the free–running values and ϕ_1 and ϕ_2 are the phase values at the observation nodes, where the two AGs are connected. To obtain the synchronized–solution curves, one must split (5) into real and imaginary parts and solve for ΔV_1 in terms of $\Delta\omega_1$ and for ΔV_2 in terms of $\Delta\omega_2$. For the input power P_{in} = –20 dBm, one obtains the ellipsoidal curves in Fig. 6(a). Measurements are also shown. The amplitude discrepancy is because (5) considers voltages at the AG nodes and measurements are carried out at the injection nodes. Note that it was not possible to obtain the synchronization curves in HB, even when using the AGs. The experimental phase noise in injection–locked conditions at f_1 = 2.3 GHz and f_2 = 4.1 GHz is shown in Fig. 6(b).

Under input signals of small amplitude, the injection–locked oscillator behaves in a near–linear manner about the free–running solution. Thus, it should be able to follow an AM modulation, as in [7]. Disregarding for simplicity the impact of one oscillation over the other, the envelope–domain equation describing the response to an AM input signal is:

$$\begin{aligned}
&\frac{\partial Y^{im}_{AG,i}}{\partial \omega_i}\frac{\Delta\dot V_i(t)}{V_i+\Delta V_i(t)}+\frac{\partial Y^{r}_{AG,i}}{\partial \omega_i}\Delta\dot\phi_i(t)=\\
&-\frac{\partial Y^{r}_{AG,i}}{\partial V_i}\Delta V_i(t)-\frac{\partial Y^{r}_{AG,i}}{\partial E^r_{gi}}E_{gi}(t)\cos\phi_i(t)+\frac{\partial Y^{r}_{AG,i}}{\partial E^{im}_{gi}}E_{gi}(t)\sin\phi_i(t)=0\\
&-\frac{\partial Y^{r}_{AG,i}}{\partial \omega_i}\frac{\Delta\dot V_i(t)}{V_i+\Delta V_i(t)}+\frac{\partial Y^{im}_{AG,i}}{\partial \omega_i}\Delta\dot\phi_i(t)=\\
&-\frac{\partial Y^{im}_{AG,i}}{\partial V_i}\Delta V_i(t)-\frac{\partial Y^{im}_{AG,i}}{\partial E^r_{gi}}E_{gi}(t)\cos\phi_i(t)+\frac{\partial Y^{im}_{AG,i}}{\partial E^{im}_{gi}}E_{gi}(t)\sin\phi_i(t)=0
\end{aligned} \tag{6}$$

System (6) is solved through numerical integration. Fig. 7 shows the amplitude $V_2+\Delta V_2(t)$ when modulating the input signal at 4.1 GHz with a rectangular waveform at 2–MHz. The steady–state experimental waveform has been superimposed.

IV. Conclusion

A stability analysis of a concurrent dual–band oscillator based on a ring resonator has been presented. It is based on the the use of a characteristic determinant, which, by construction, cannot exhibit any RHS poles. The circuit can operate as a concurrent zero–IF self–oscillating mixer through the dual injection locking of the two coexistent oscillations.

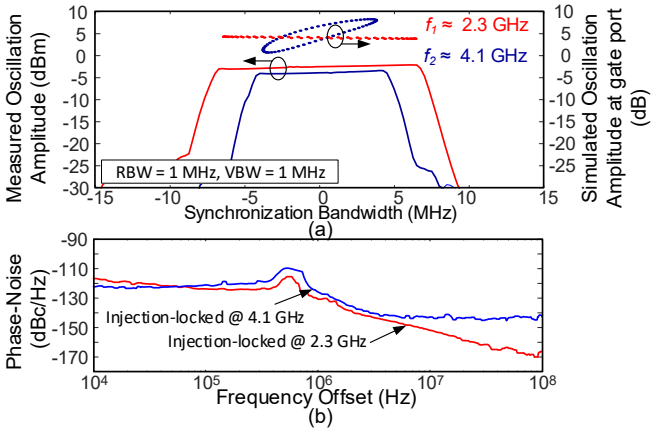

Fig. 6. Concurrent Zero–IF SOM. (a) Simulated and measured synchronization curves at the injection nodes in Fig. 1(c) using a circulator. (b) Phase–noise spectral density at f_1 = 2.3 GHz and f_2 = 4.1 GHz.

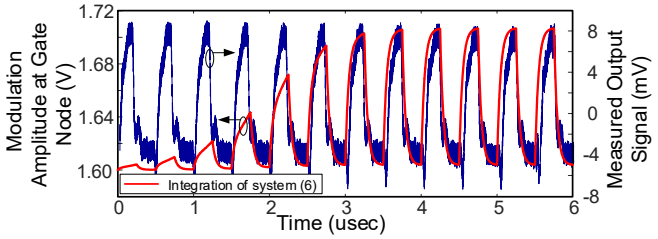

Fig. 7. Amplitude $V_2+\Delta V_2(t)$ obtained through (6), when modulating the input signal at 4.1 GHz with a rectangular waveform at 2–MHz. The steady–state experimental waveform has been superimposed.

Acknowledgment

Work supported by the Spanish Ministry of Science and Innovation (ERDF/FEDER) project TEC2017-88242-C3-1-R.

References

[1] A. Goel and H. Hashemi, "Injection locking in concurrent dual frequency oscillators," *IEEE Trans. Microw. Theory Techn.*, vol. 56, no. 8, pp. 1834–1845, Aug. 2008.

[2] U. L. Rohde and A. K. Poddar, "Concurrent, reconfigurable, and adaptable oscillators for multi–band multi–mode communication systems," *Proc. 37th Eur. Microw. Conf.*, Oct. 2007, pp. 292–295.

[3] J. S. Schaffner, "Simultaneous oscillations in oscillators", *Trans. of the IRE*, vol.CT–1, no.2, pp.2–8, June 1954.

[4] F. Ramírez, S. Sancho and A. Suárez, "Oscillation Modes in Multiresonant Oscillator Circuits," *IEEE Trans. Microw. Theory Techn*, vol. 64, no. 12, pp. 4660–4675, Dec. 2016.

[5] B. Li, Y. Liu, C. Yu and Y. Wu, "A Novel Concurrent Dual–Band Oscillator Based on a Single Ring Resonator," *IEEE Microw. Wireless Comp. Lett.*, vol. 26, no. 8, pp. 607–609, Aug. 2016.

[6] J. Jugo, J. Portilla, A. Anakabe, A. Suarez, and J. M. Collantes, "Closed loop stability analysis of microwave amplifiers," *Electron. Lett.*, vol. 37, no. 4, pp. 226–228, Feb. 2001.

[7] P. Burasa, N. G. Constantin and K. Wu, "Low–Power Injection–Locked Zero–IF Self–Oscillating Mixer for High Gbit/s Data–Rate Battery–Free Active uRFID Tag at Millimeter–Wave Frequencies in 65–nm CMOS," *IEEE Trans Microw. Theory Techn.*, vol. 64, no. 4, pp. 1055–1065, 2016.

[8] A. Suárez and F. Ramírez, "Stability and Bifurcation Analysis of Multi–Element Non–Foster Networks *IEEE Trans. Microw. Theory Techn.*, vol. 66, no. 4, pp. 1817–1830, 2018.

[9] A. Suárez, R. Quéré, *Stability Analysis of Nonlinear Microwave Circuits*, Artech–House Publishers, Boston, 2003.

[10] S. Hernández, M. Pontón and A. Suárez, "Simulation Method for Complex Multivalued Curves in Injection–Locked Oscillators," *IEEE Trans. Microw. Theory Techn.*, vol. 65, no. 11, pp. 4046–4062, 2017.